THE JOURNAL OF PHYSICAL CHEMISTRY A
A JOURNAL OF THE AMERICAN CHEMICAL SOCIETY

pubs.acs.org/JPCA

Article

Unraveling the Rich Fragmentation Dynamics Associated with S−H Bond Fission Following Photoexcitation of H_2S at Wavelengths ∼129.1 nm

Published as part of The Journal of Physical Chemistry A virtual special issue "Xueming Yang Festschrift."

Zijie Luo, Yucheng Wu, Shuaikang Yang, Zhenxing Li, Wei Hua, Zhichao Chen, Li Che, Xingan Wang, Michael N. R. Ashfold,* and Kaijun Yuan*

Cite This: *J. Phys. Chem. A* 2024, 128, 3351−3360

Read Online

ACCESS | Metrics & More | Article Recommendations | Supporting Information

ABSTRACT: H_2S is being detected in the atmospheres of ever more interstellar bodies, and photolysis is an important mechanism by which it is processed. Here, we report H Rydberg atom time-of-flight measurements following the excitation of H_2S molecules to selected rotational (J_{KaKc}') levels of the $^1B_1$ Rydberg state associated with the strong absorption feature at wavelengths of $\lambda \sim 129.1$ nm. Analysis of the total kinetic energy release spectra derived from these data reveals that all levels predissociate to yield H atoms in conjunction with both SH(A) and SH(X) partners and that the primary SH(A)/SH(X) product branching ratio increases steeply with $\langle J_b^2 \rangle$, the square of the rotational angular momentum about the *b*-inertial axis in the excited state. These products arise *via* competing homogeneous (vibronic) and heterogeneous (Coriolis-induced) predissociation pathways that involve coupling to dissociative potential energy surfaces (PES(s)) of, respectively, $^1A''$ and $^1A'$ symmetries. The present data also show H + SH(A) product formation when exciting the $J_{KaKc}' = 0_{00}$ and 1_{11} levels, for which $\langle J_b^2 \rangle = 0$ and Coriolis coupling to the $^1A'$ PES(s) is symmetry forbidden, implying the operation of another, hitherto unrecognized, route to forming H + SH(A) products following excitation of H_2S at energies above ∼9 eV. These data can be expected to stimulate future *ab initio* molecular dynamic studies that test, refine, and define the currently inferred predissociation pathways available to photoexcited H_2S molecules.

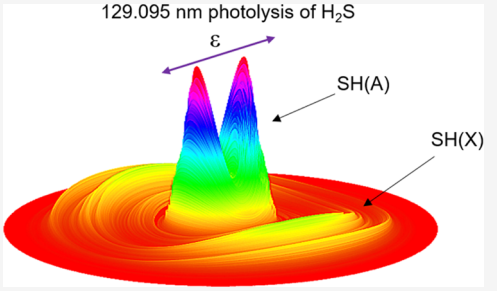

1. INTRODUCTION

Sulfur is the fifth most abundant volatile element in our solar system,[1] but the relative abundances of S-containing species detected in the interstellar medium (ISM) vary greatly. The densities of such species in low-density, diffuse clouds are estimated at close to the cosmic value,[2] but studies in denser regions of the ISM typically return significantly lower fractional abundance estimates.[3−5] The estimated abundances in the outer layers of the photodissociation region in the Horsehead nebula, for example, are only about a quarter of the cosmic value,[6] and the values in cold molecular clouds are much lower still.[7−9] This reduction has been rationalized by assuming that much of the (undetected) sulfur is incorporated in dust grains and icy mantles. The abundance and mobility of hydrogen in an ice matrix encourage the view that most of the sulfur released from interstellar ice mantles (by sputtering and thermal and/or photoinduced desorption) will be in the form of H_2S.[10−13] The detections of H_2S in the coma of P/Halley,[14] C/1995 O1 (Hale-Bopp),[15,16] C/2014 Q2 (Lovejoy),[17] and 67P/Churyumov−Gerasimenko[18] accord with such expectations. H_2S has also been detected in the atmospheres of Jupiter,[19] Uranus,[20,21] and Neptune,[22] in protoplanetary disks in Taurus,[23] in an isolated massive protostar,[24] and in a brown dwarf[25] and has recently proposed as a source of sulfur in the hotter, denser atmospheres of exoplanets like Wasp-39b, where its photochemical processing is predicted to contribute to the detected SO_2.[26]

Photodissociation is an important destruction process for H_2S molecules in low-density regions of the ISM. As Figure 1 shows, the electronic spectrum of H_2S exhibits two regions of broad continuous absorption, one centered at wavelengths $\lambda \sim 195$ nm and the second of which becomes increasingly evident at $\lambda < 150$ nm.[27] Many intense, narrow bands sit on top of the shorter wavelength continuum.[28,29] These are signatures of excitations to Rydberg states, belonging to series that converge to the first ionization limit (84 432 ± 2 cm^{-1} (ref 30)).

Received: March 6, 2024
Revised: April 12, 2024
Accepted: April 15, 2024
Published: April 23, 2024

https://doi.org/10.1021/acs.jpca.4c01478
J. Phys. Chem. A 2024, 128, 3351−3360

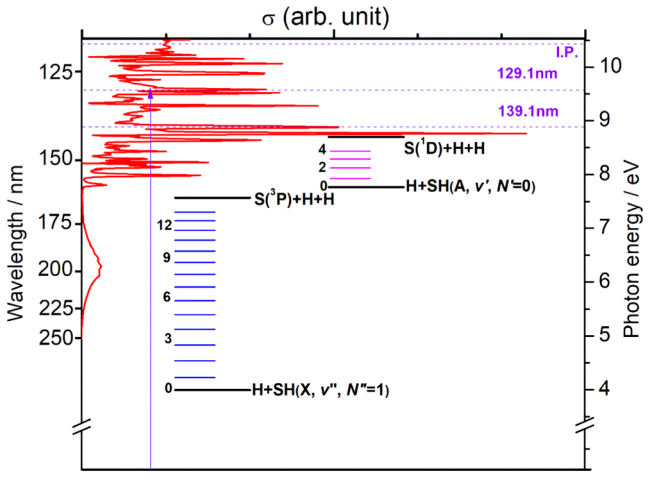

Figure 1. H_2S absorption cross section versus wavelength (after ref 27), with the 129.1 and 139.1 nm features highlighted, along with the energetic thresholds for each of dissociation channels I–IV, for ionization (I.P.), and for forming SH(X) and SH(A) products in different vibrational states.

Formation of ground-state H_2S^+ involves the removal of an electron from the nonbonding $2b_1$ orbital (essentially the S $3p_x$ orbital) of the neutral molecule. This causes a negligible change in equilibrium geometry, and the associated Franck–Condon factors thus ensure that the absorption to each of these Rydberg states is dominated by the origin band (i.e., the $v' = 0 \leftarrow v'' = 0$ transition). Several of these Rydberg states are sufficiently long-lived (i.e., predissociate sufficiently slowly) that their spectra show resolved rotational fine structure.[28,29,31,32]

Table 1 shows threshold energies for the various spin-allowed fragmentation channels of H_2S molecules at the photolysis wavelength of particular interest in the present work. The threshold energies for channels I–IV are also included in Figure 1, along with the vibrational energies of the SH products. Prior experimental (photofragment translational spectroscopy (PTS))[38,39] studies and *ab initio* electronic structure calculations[40] have determined that the long wavelength continuum arises *via* excitation to two coupled states of $^1A''$ symmetry (in the C_s point group, with $^1B_1$ and $^1A_2$ symmetries in C_{2v}). Photoexcitation within this continuum yields H + SH(X) products, and the internal (rovibrational) excitation of the SH fragments increases with a decreasing excitation wavelength. Richer photochemistry including all channels I to VI has been identified when exciting at wavelengths shorter than ~150 nm,[41] where the higher energy ($^1A'$) continuum can be accessed directly, by nonadiabatic coupling following the initial population of the Rydberg states. The Rydberg states can also decay by radiationless coupling to the $^1A''$ continuum, and theory and experiment have identified nonadiabatic coupling routes (*e.g.* conical intersections, Renner–Teller seams of intersection) by which population can funnel between the states responsible for the $^1A'$ and $^1A''$ continua.[41]

Table 1. Thermochemical Threshold Energies for Spin-Allowed Fragmentation Channels I–VI of H_2S, Derived Using Literature Values for the Bond Dissociation Energies $D_0°(HS–H)$,[33] $D_0°(S–H)$,[34] and $D_0°(H–H)$,[35] and the Term Values $T_{00}(SH(A–X))$,[36] $\Delta E(S(^1D_2–^3P_2))$, and $\Delta E(S(^1S_0–^3P_2))$[37]

channel	fragments	threshold energy/cm^{-1}
I	$H + SH(X^2\Pi_{3/2}, v'' = 0, N'' = 1)$	31 451 ± 4
II	$H + SH(A^2\Sigma^+, v' = 0, N' = 0)$	62 284 ± 4
II′	$SH(A^2\Sigma^+, v, N) \rightarrow H + S(^3P_J)$, $(J = 2, 1, 0)$	
III	$H + H + S(^3P_J)$, $(J = 2, 1, 0)$	60 696 ± 25[a]
IV	$H + H + S(^1D_2)$	69 935 ± 25
V	$H_2(X^1\Sigma_g^+, v'' = 0, J'' = 0) + S(^1D_2)$	33 817 ± 25
VI	$H_2(X^1\Sigma_g^+, v'' = 0, J'' = 0) + S(^1S_0)$	46 758 ± 25

[a]The reported threshold energy for channel III is for forming $S(^3P_2)$ products.

The present study focuses on S–H bond fission processes following excitation to one Rydberg state, responsible for the strong absorption feature at $\lambda \sim 129.1$ nm. Previous band contour analyses have established that the excited state has $^1B_1$ symmetry (in C_{2v}), and its associated quantum defect ($\delta \sim 0.03$, assuming $n = 4$) has encouraged assignment in terms of a $4da_1 \leftarrow 2b_1$ orbital promotion.[28,29] Recent studies employing vacuum ultraviolet (VUV) photons from the free electron laser (FEL) at the Dalian Coherent Light Source (DCLS) to excite the band and PTS methods (H atom Rydberg tagging time-of-flight (HRTOF) or time-sliced velocity map ion imaging methods) to measure the translational energy distributions of the resulting H,[41,42] $S(^1D)$,[42] and $S(^1S)$[43] photoproducts have confirmed that channels I to VI are all active at this wavelength, with channels I and II, involving fission of one S–H bond, the dominant primary processes. Every SH(A) photoproduct will predissociate to yield a second H atom (channel II′ in Table 1) within, at most, a few nanoseconds of its formation.[44,45] These secondary H atoms are also detected in the PTS experiments, so channels II and II′ together constitute a sequential contribution to the overall channel III.

The bandwidth of the VUV-FEL source spans much of any one Rydberg feature in the absorption spectrum of a jet-cooled H_2S sample, thus precluding investigation of the ways in which the photofragmentation dynamics depend on the parent rotational state. Here, we report higher resolution studies of rotational (*i.e.* J_{KaKc}') level-dependent predissociation dynamics of the $^1B_1$ Rydberg state responsible for the strong absorption feature of H_2S at $\lambda \sim 129.1$ nm. The new data are compared with those returned by recent studies of the first ($3da_1 \leftarrow 2b_1$) member of the same Rydberg series[46] (responsible for a strong absorption at $\lambda \sim 139.1$ nm), thereby revealing some of the consequences of accessing the various dissociation continua from a very similar starting geometry but at a higher ($\Delta E \sim 5500$ cm^{-1}) absolute excitation energy.

2. EXPERIMENTAL METHODS

The product total translational energy, $P(E_T)$, distributions were obtained using tunable VUV pump and probe sources along with HRTOF detection.[47] The experimental apparatus and methods have been detailed previously.[46,48–51] The H_2S sample (typically 30% seeded in Ar) was introduced into the interaction volume in the form of a pulsed jet. The photolysis photons at $\lambda \sim 129.1$ nm were generated by difference four-wave mixing (DFWM) involving two $\lambda = 212.556$ nm photons, and one $\lambda \sim 600$ nm photon overlapped in a stainless-steel cell filled with a 3:1 ratio Ar/Kr gas mixture. The wavelengths of all laser outputs used in this study were established using a wavemeter. The HRTOF spectra were recorded along axes at angles $\theta = 0°$ (parallel), 90° (perpendicular), and 54.7° (i.e., at

https://doi.org/10.1021/acs.jpca.4c01478
J. Phys. Chem. A 2024, 128, 3351–3360

the magic angle) to the electric ($\boldsymbol{\varepsilon}$) vector of this VUV radiation, using a rotatable half-waveplate to rotate the $\boldsymbol{\varepsilon}$ vector of the tunable ($\lambda \sim 600$ nm) radiation. The VUV probe photons at the H Lyman-α wavelength ($\lambda = 121.6$) were also generated by DFWM, in another cell containing a 3:1 Ar/Kr gas mixture, mounted on the opposite side of the photolysis chamber, employing two $\lambda = 212.556$ nm photons along with a $\lambda \sim 845$ nm photon. The resulting H($n = 2$) atoms were promoted to a high-n ($n = 30-80$) Rydberg state, lying just below the ionization threshold, by absorbing a further photon with $\lambda \sim 365$ nm. Background signals that could arise from $\lambda = 212.556$ nm photolysis of H_2S in the interaction region were eliminated by arranging that the various beams passed through a biconvex LiF lens positioned off-axis at the exit of each Ar/Kr gas cell, thereby ensuring that only the VUV beam was dispersed through the interaction region.[52] The 121.6 nm photons also induce H_2S photolysis and thus generate H atom signals. To counter this, a background subtraction method was employed, with the photolysis laser radiation only present on alternate probe laser shots.

The Rydberg-tagged H atom photofragments flew a known distance, $d \sim 280$ mm, prior to striking a grounded mesh mounted close in front of a Z-stack microchannel plate detector where they were field-ionized by the ~2000 V cm^{-1} electric field. The detected signal was then passed to a fast preamplifier and counted by a multichannel scaler. The recorded TOF data were converted to the corresponding H atom translational energy distributions and momentum arguments then used to derive corresponding $P(E_T)$ distributions, as described previously.[47] H atom photofragment excitation (PHOFEX) spectra were recorded by integrating the H atom signal while scanning through the requisite range of photolysis wavelengths.

3. RESULTS AND DISCUSSION

3.1. H Atom PHOFEX Spectrum. Figure 2A shows the excitation spectrum for forming H atoms following the excitation of a jet-cooled sample of H_2S across the wavenumber range of 77 380−77 510 cm^{-1} (129.23−129.02 nm). Each feature can be assigned to one or more lifetime broadened $J_{KaKc}'-J_{KaKc}''$ transitions using the spectral simulation program PGOPHER[53] together with appropriate spectroscopic parameters. The ground-state constants were taken from the literature,[54] and excited-state constants identical to those for the ground-state ion[55] were assumed. The resulting simulation is shown in stick form, with each transition assigned a line width, in Figure 2B. This sufficed to assign the dominant contributors to the various maxima in the PHOFEX spectrum (labeled 1 and 8 in Figure 2A) and to establish the $^1B_1-X^1A_1$ band origin ($\nu_0 = 77\,444$ cm^{-1}). This analysis identifies feature 2 at $\lambda = 129.158$ nm (77 424.5 cm^{-1}) as a single rovibronic transition (the $0_{00}-1_{10}$ line), that feature 5 at $\lambda = 129.095$ nm (77 462.3 cm^{-1}) is dominated by the $1_{10}-0_{00}$ transition, and that the $2_{11}-1_{01}$ transition is the major contributor to the blended feature 6 centered at 129.068 nm (77 478.5 cm^{-1}). Table 2 provides a fuller description of the stronger transitions contributing to each of features 1−8 (highlighted in the stick spectrum in Figure 2B) and the values of $\langle J_b^2\rangle$, the expectation value of the square of the angular momentum about the b-inertial axis in the various excited rotational levels.

Several factors influence the relative intensities of the various spectral features. Each rotational level of H_2S satisfies either

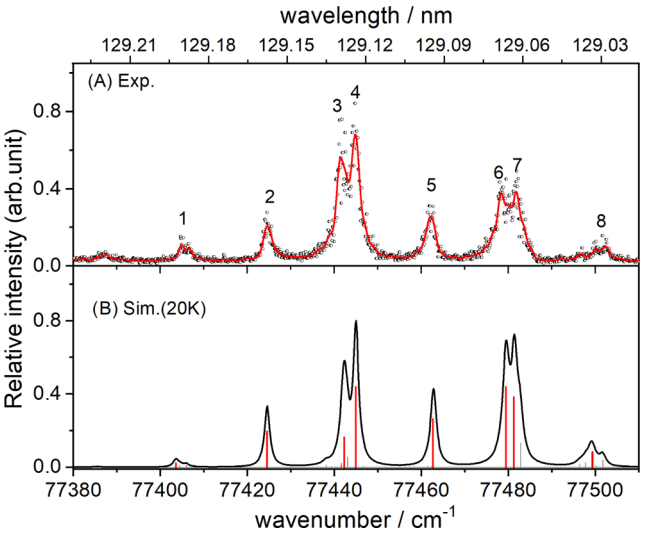

Figure 2. (A) H atom PHOFEX spectrum recorded using a jet-cooled 30% H_2S in Ar gas mixture. (B) PGOPHER simulation of the $H_2S(^1B_1-X^1A_1)$ assuming spectroscopic parameters from refs 54 and 55 and a band origin $\nu_0 = 77\,444$ cm^{-1}. The simulated spectrum is shown both in stick form and with each rovibronic transition clothed with a (Lorentzian) line shape with a full width at half-maximum (fwhm) determined by the excited-state lifetime. The widths are modeled as the sum of homogeneous and heterogeneous contributions, using the function $\omega = \omega_0 + \omega'\langle J_b^2\rangle$ with $\omega_0 = 1.5$ cm^{-1} and $\omega' = 0.1$ cm^{-1}. The peak amplitude in each case is reduced in a compensatory manner to conserve the rovibronic transition line strength. The simulation assumes rotational and nuclear spin temperatures $T_{rot} = 20$ K and $T_{ns} = 300$ K, respectively.

Table 2. Measured Wavelengths/Wavenumbers of Maxima in the H Atom PHOFEX Spectrum (Figure 2A) and the Dominant Contributing Transitions Identified by the PGOPHER Simulation (Figure 2B)[a]

peak	measured wavelength/nm	wavenumber/cm^{-1}	transition	$\langle J_b^2\rangle$
1	129.191	77 404.8	$\mathbf{1_{11}-2_{21}}$	0
2	129.158	77 424.5	$\mathbf{0_{00}-1_{10}}$	0
3	129.130	77 441.3	$\mathbf{2_{02}-2_{12}}$	1.48
			$1_{01}-1_{11}$	1
4	129.124	77 444.9	$\mathbf{1_{11}-1_{01}}$	0
5	129.095	77 462.3	$1_{10}-0_{00}$	1
6	129.068	77 478.5	$\mathbf{2_{11}-1_{01}}$	4
7	129.064	77 480.9	$\mathbf{2_{20}-1_{10}}$	2.518
8	129.029	77 502.0	$\mathbf{3_{22}-2_{12}}$	4

[a]The transitions of *ortho*-H_2S molecules are highlighted in bold, and the final column shows $\langle J_b^2\rangle$, the expectation values of the square of the angular momentum about the b-inertial axis for the various excited rotational levels.

ortho- or *para*-nuclear spin statistics. The *ortho*-levels (for which $K_a + K_c$ = odd in the $\tilde{X}$ state) have 3 times higher statistical weight, and transitions involving *ortho*-H_2S molecules are highlighted in bold in Table 2. The *ortho*- and *para*-H_2S molecules do not interconvert during the supersonic expansion, so any simulation of the jet-cooled excitation spectra must employ different rotational (T_{rot}) and nuclear spin (T_{ns}) temperatures. The simulated spectrum in Figure 2B assumes $T_{rot} = 20$ K and $T_{ns} = 300$ K.

The excitation spectrum for forming H atom products (Figure 2A) reports some convolution of the parent absorption cross section and the branching ratio for dissociating to yield

https://doi.org/10.1021/acs.jpca.4c01478
J. Phys. Chem. A 2024, 128, 3351−3360

one or more H atoms. The H_2 elimination channels V and VI (Table 1) are both minor processes at the wavelengths of current interest,[41] so it is logical to compare the H atom PHOFEX spectrum with the predicted parent absorption spectrum (Figure 2B). Three further features merit note, however. First, the signal intensity in the H atom PHOFEX spectrum (Figure 2A) does not fall to zero between the peaks, consistent with the underlying background absorption evident in the parent absorption spectrum (Figure 1). The PGOPHER simulation, in contrast, reports only the absorptions associated with the $^1B_1$–X^1A_1 transition. Second, as in the case of the $^1B_1$ state arising from the $3da_1 \leftarrow 2b_1$ promotion at $\lambda \sim 139.1$ nm,[46] the simulation shown in Figure 2B also recognizes that the excited state J_{KaKc}' levels can predissociate by both homogeneous and heterogeneous (i.e., rotational level independent and dependent) mechanisms and that the rate of the latter (Coriolis-driven) predissociation scales with $\langle J_b^2 \rangle$. The parameters used in the present simulation are included in the caption of Figure 2. Finally, the analysis of the present $P(E_T)$ spectra (see below) and previous studies[41] show that the *b*-axis rotationally induced predissociation of H_2S Rydberg states with $^1B_1$ symmetry enables coupling to the $^1A'$ continuum and favors dissociation to H + SH(A) products (channel II). The resulting SH(A) products predissociate (channel II′), so the net effect is the formation of two H atoms per absorbed photon. Peaks in the H atom PHOFEX spectrum associated with transitions to J_{KaKc}' levels with higher $\langle J_b^2 \rangle$ can thus be expected to appear with enhanced intensity, *cf.* the PGOPHER simulation.

3.2. H Atom TOF and $P(E_T)$ Distributions. The data selected for presentation in this section are from excitation on peaks 2, 5, and 6, which span a representative range of excited-state $\langle J_b^2 \rangle$ values. Equivalent data obtained following excitation on the other features labeled in Figure 2A are displayed in Figure S1 in the Supporting Information.

Figure 3 shows HRTOF spectra measured when exciting on these three lines, which sample (predominantly or exclusively) the 0_{00}, 1_{10}, and 2_{11} excited-state levels with, respectively, $\langle J_b^2 \rangle$ = 0, 1, and 4. These spectra immediately show the switch in the relative intensities of the early and later TOF (high and low E_T) components with increasing $\langle J_b^2 \rangle$ and the very different recoil anisotropies of the high and low E_T products, particularly when exciting to the 1_{10} level *via* line 5 (panel B). Similarly dramatic product state-dependent recoil anisotropies have been noted previously when exciting the 1_{10}–0_{00} line in the origin bands of the C^1B_1–X^1A_1 transition of H_2O[56] and of the $^1B_1$–X^1A_1 transition of H_2S at $\lambda \sim 139.1$ nm.[46]

The HRTOF data can be placed on a more quantitative footing by conversion to the corresponding $P(E_T)$ distributions. The spectrum obtained when exciting the 0_{00} level (Figure 4A) shows signal out to $E_T \sim 45\,000$ cm^{-1}, indicative of the formation of H + SH(X) fragments in a wide range of v'', N'' levels spanning all the way from $v'' = 0$, and low N'' up to (and beyond) the three-body dissociation limit III. Such SH(X, v'', N'') population distributions have been reported previously when exciting at similar VUV wavelengths;[41] the observation of signal at E_T values in the window between the thermochemical onsets for channels II and III implies the formation of some SH(X) fragments in very high N'' levels, which survive by virtue of the associated centrifugal potential. H + SH(X) product formation in this case is explained by homogeneous vibronic coupling from the $^1B_1$ state to the $^1A''$ continuum. But Figure 4A also shows the distinctive signature

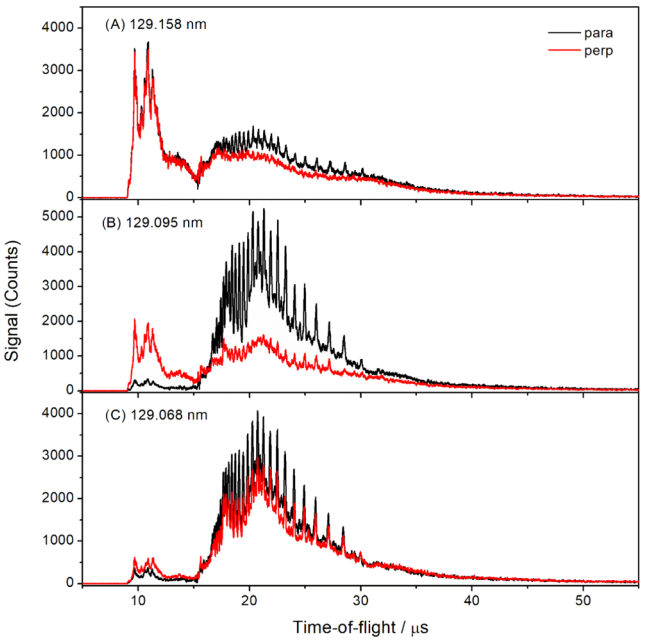

Figure 3. H atom TOF spectra obtained following photolysis of a jet-cooled 30% H_2S in Ar sample at (A) 129.158 nm, (B) 129.095 nm, and (C) 129.068 nm, sampling predominantly or exclusively the 0_{00}, 1_{10}, and 2_{11} excited-state levels. Data measured with the $\boldsymbol{\varepsilon}$ vector of the photolysis laser radiation aligned parallel (θ = 0°) and perpendicular (θ = 90°) to the detection axis are shown in black and red, respectively.

of H + SH(A) fragments at low E_T and, as at other neighboring wavelengths, the SH(A) fragments include a significant fraction in "super-rotor" levels, i.e., quasi-bound levels above the thermochemical threshold for dissociation to H + S(^{1}D) products supported by the accompanying centrifugal potential energy barrier. We return to address the gross SH(A) product yield observed at this wavelength in Section 3.4, after considering the $P(E_T)$ data obtained when exciting the other lines in the H atom PHOFEX spectrum (Figure 2A) and the quantum state population distributions that they reveal.

Figure 4B,C shows, respectively, the $P(E_T)$ spectra obtained when exciting to the 1_{10} and 2_{11} levels. These clearly demonstrate that increasing $\langle J_b^2 \rangle$ translates into higher SH(A)/SH(X) product ratios. This trend is confirmed by the spectra shown in Figure S2: the relative yield of SH(A) fragments is much higher when exciting line 8 (λ = 129.029 nm, $\langle J_b^2 \rangle \sim 4$), for example, than when exciting line 4 (λ = 129.124 nm, $\langle J_b^2 \rangle = 0$). Again, a substantial fraction of the SH(A) products is formed in $v' = 0$, very high N', "super-rotor" levels, with N' values up to at least 39. The present data also show clear steps at E_T values appropriate for forming SH(A) fragments in levels with $v' > 0$ (most obviously, v' = 1 and 2) and low N'.

As noted in Section 1, all SH(A) radicals predissociate on a nanosecond (or shorter) time scale to yield H + S(^3P_J) atom products.[44,45] Thus, the primary SH(A) photoproducts revealed in Figure 4 must decay to yield a second H atom within the time that the Rydberg tagging laser radiation is present, and these secondary H atoms must also contribute to the total $P(E_T)$ spectra. The predissociation of SH(A, $v' = 0$) radicals favors population of ground (J = 2) spin–orbit state S(^3P_J) products,[44,57] and an illustrative comb indicating the E_T values of H + S($^3P_2$) products expected from predissociation of

https://doi.org/10.1021/acs.jpca.4c01478
J. Phys. Chem. A 2024, 128, 3351−3360

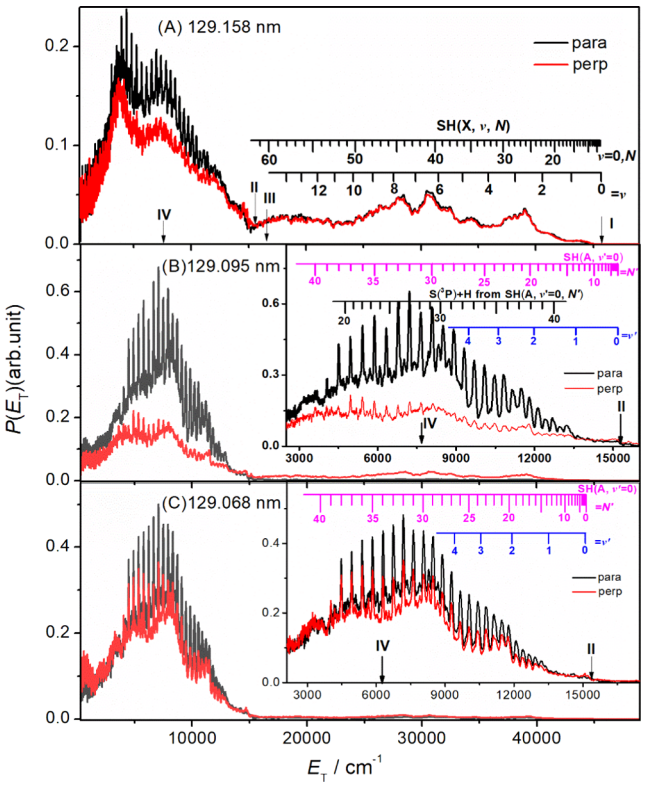

Figure 4. $P(E_T)$ spectra derived from H atom TOF spectra following photodissociation of H_2S at (A) 129.158 nm, (B) 129.095 nm, and (C) 129.068 nm with $\boldsymbol{\varepsilon}$ aligned, respectively, parallel (θ = 0°, black) and perpendicular (θ = 90°, red) to the detection axis. The vertical arrows and combs in (A) show the maximum E_T values associated with H atom formation *via* channels I–IV, and the E_T values associated with the formation of H plus SH(X) fragments in selected v'', N'' levels. The insets in panels (B) and (C) show expanded views of the lower E_T region, with the superposed combs defining the E_T values associated with the formation of H plus SH(A) fragments in selected v', N' levels.

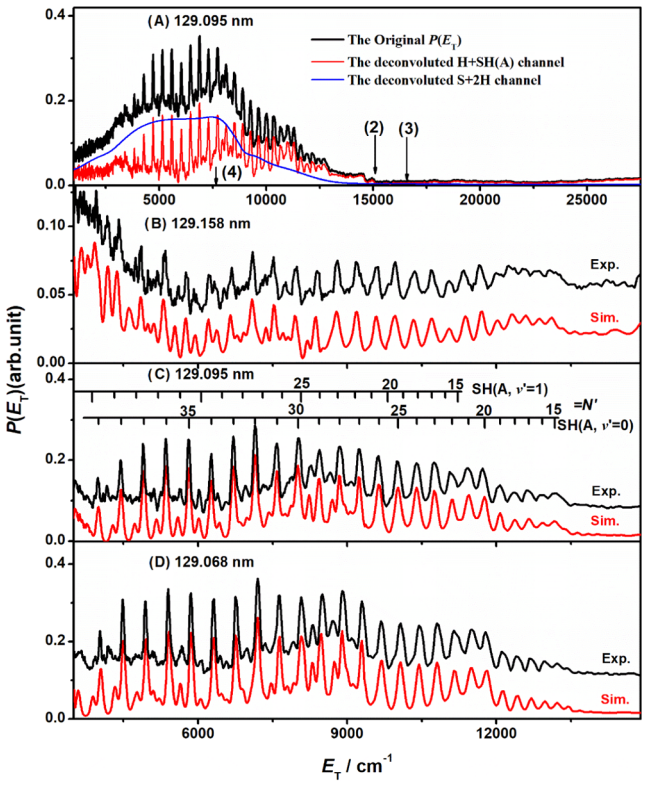

Figure 5. (A) Illustration of the $P(E_T)$ spectrum obtained following photodissociation of H_2S at 129.095 nm with $\boldsymbol{\varepsilon}$ aligned at θ = 54.7° to the detection axis and its deconvolution into components attributable to primary dissociation to H + SH(A) products (channel II, red) and to secondary decay of SH(A) products plus three-body dissociation (channels II′, III, and IV, blue). The remaining three panels show simulations (red) of the primary spectra obtained by deconvoluting $P(E_T)$ data (black) following excitation at (B) 129.158 nm, (C) 129.095 nm, and (D) 129.068 nm and then varying the populations ascribed to different SH(A, v', N') levels. The red and black traces have been offset vertically in panels (B), (C), and (D) for ease of display.

selected SH(A, v' = 0, N') photoproducts is also included in the inset in Figure 4B. Finally, we note that in all cases, the signal intensity is declining at the lowest E_T, reinforcing the view that the simultaneous three-body dissociation to H + H + S(^{1}D) products (channel IV) is at most a minor channel.

3.3. Estimating SH(A) Product Population Distributions and the S/SH Product Branching Ratios. Figure 5A presents a deconvolution of the low E_T part of the $P(E_T)$ spectrum obtained at λ = 129.095 nm (θ = 54.7°, magic angle data, to remove recoil anisotropy effects) into components attributable to primary dissociation to H + SH(A) products (channel II) and to secondary decay of the primary SH(A) fragments into H + S(^3P_J) products (channel II′). The simultaneous three-body dissociations from channels III and IV also contribute to the low E_T part of the $P(E_T)$ spectrum but with a minor proportion according to previous studies.[58] Inevitably, there is some arbitrariness associated with this deconvolution, but the trends revealed are robust. The kinetic energies of the secondary H atoms are necessarily less tightly constrained given the spread of primary SH(A) recoil directions and the fact that the SH(A) products can predissociate into more than one spin–orbit state. Thus, the complete $P(E_T)$ spectrum is viewed as a sum of a "sharp" primary H + SH(A) spectrum and a less well-resolved envelope of similar area derived from the secondary decay of these SH(A) products.

Figure 5A shows a plausible envelope for the three-body dissociation (i.e., channels II′, III, and IV) products formed at this wavelength (in blue), and the primary H + SH(A) spectrum (in red) obtained by subtracting this envelope from the full $P(E_T)$ spectrum. Figure 5C shows a simulation of the deduced primary spectrum, obtained by varying the populations ascribed to different SH(A, v', N') levels. The deduced product vibrational, $P(v')$, distribution is shown in Figure 6B, and the rotational population distribution associated with the majority v' = 0 products (the $P(v'$ = 0, $N')$ distribution) is shown in Figure 6E. Corresponding simulations of the deconvolved primary H + SH(A) spectra obtained at λ = 129.158 and 129.068 nm are shown in Figure 5B,D, and analogous plots for deconvolved data obtained at four of the other five excitation wavelengths are shown in Figure S3 (the low E_T part of the spectrum obtained at λ = 129.124 nm was insufficiently resolved for reliable deconvolution). The visual agreement in all cases is pleasing, but we reiterate the point that none of the deconvolutions is likely to be a unique solution to the data. The derived $P(v')$ and $P(v'$ = 0, $N')$ distributions obtained at λ = 129.158 and 129.068 nm are shown in, respectively, Figure 6A,D, and 6C,F, and the

https://doi.org/10.1021/acs.jpca.4c01478
J. Phys. Chem. A 2024, 128, 3351–3360

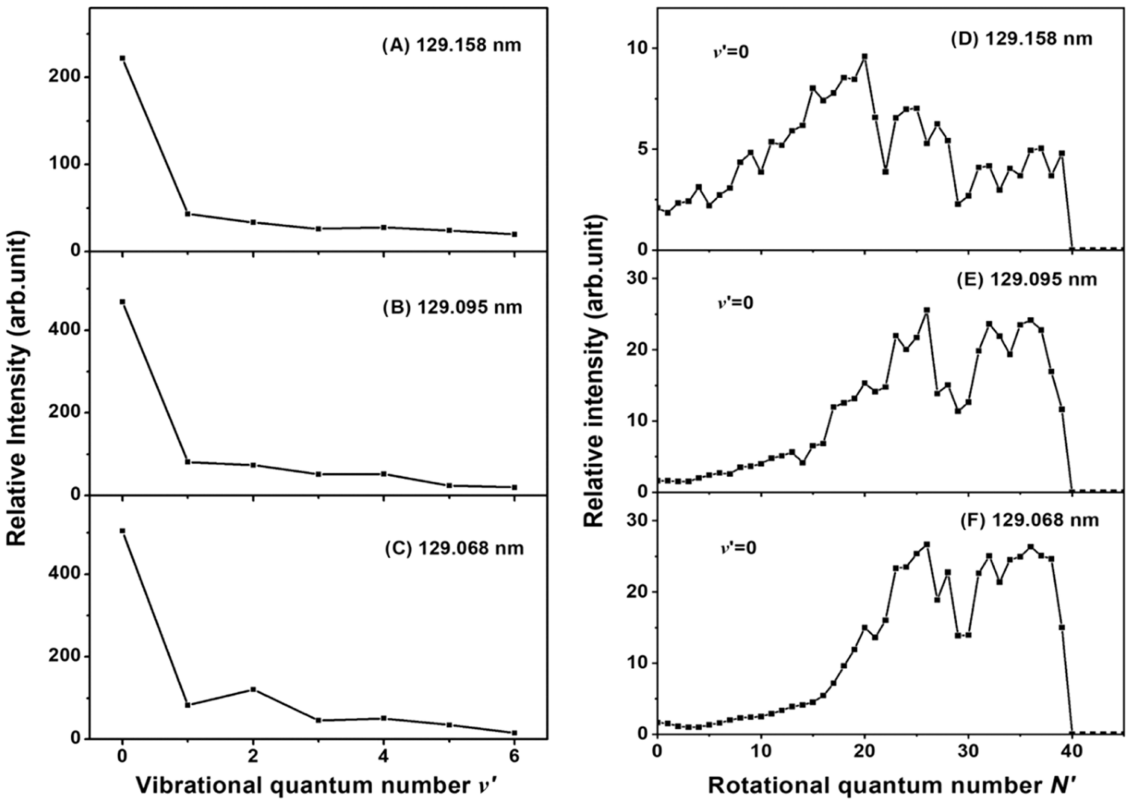

Figure 6. SH(A) product vibrational, $P(v')$, distributions and the rotational population distributions of the majority $v' = 0$ products (the $P(v' = 0, N')$ distributions) obtained following photodissociation of H_2S at λ = (A, D) 129.158 nm, (B, E) 129.095 nm, and (C, F) 129.068 nm derived from the simulations shown in Figure 5.

corresponding distributions obtained at all other excitation wavelengths apart from λ = 129.124 nm are shown in Figure S4.

Inspection of Figures 6 and S4 shows that ∼60% of the SH(A) fragments are in their $v' = 0$ level and that these fragments are formed with a highly inverted rotational state distribution. Careful inspection of Figure 5C, in particular, shows features attributable to the formation of SH(A, $v' = 1$ high N') levels also, illustrated by the additional comb shown in that figure. Broadly similar energy disposal has been found in previous studies at neighboring wavelengths. For example, a similar simulation of the low E_T part of the $P(E_T)$ spectrum obtained at λ = 139.015 nm suggests that >80% of the primary SH(A) fragments are formed in their $v' = 0$ level with an inverted rotational state population distribution extending to $N' \sim 32$,[46] and SH(A, $v' = 0$) fragments with an inverted rotational population distribution stretching to $N' \leq 41$ were identified in the earlier studies of H_2S photolysis at the H Lyman-α wavelength.[59,60] In all such cases, the high product rotational excitation has been explained in terms of the photoexcited parent molecules coupling to the $^1A'$ continuum, where the balance of bending (toward and beyond linearity) and asymmetric stretching forces arising from the topography of the potential energy surface (PES) manifests as massive product rotational excitation in the asymptotic SH(A) products.[41]

This analysis also allows estimation of the relative yields of primary H + SH(A) (channel II) and H + SH(X) (channel I) products at the various excitation wavelengths and thus as a function of parent J_{KaKc}' level. In each case, the magic angle $P(E_T)$ spectrum was split at the E_T value corresponding to the onset for channel II, E_T(II), and the integrated intensity of the deconvolved channel II signal shown in Figure 5 was compared with that of the total signal with $E_T > E_T$(II). It is noted that every SH(A) radical and its subsequent dissociation correlate with two H atom products. As Figure 7 shows, the primary SH(A)/SH(X) yield increases rapidly with increasing $\langle J_b^2 \rangle$, as expected given that b-axis rotation has the appropriate symmetry to enable Coriolis coupling with the $^1A'$ continuum

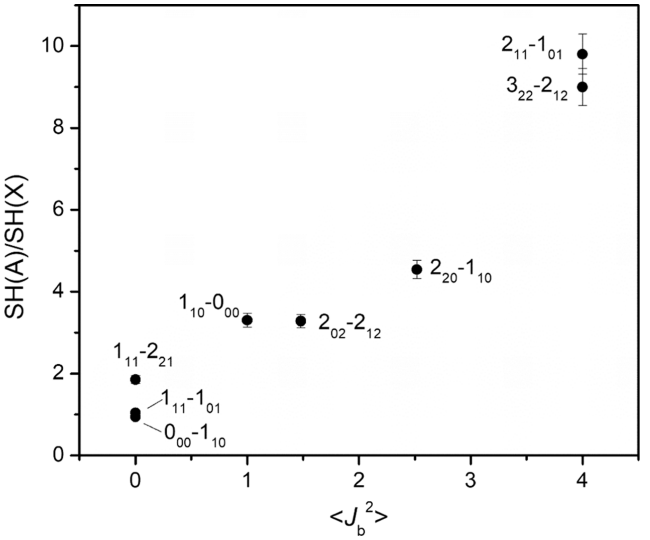

Figure 7. Plot showing the deduced primary SH(A)/SH(X) (or S/SH) yield as a function of $\langle J_b^2 \rangle$ for the J_{KaKc}' levels accessed by the various transitions investigated in this work.

https://doi.org/10.1021/acs.jpca.4c01478
J. Phys. Chem. A 2024, 128, 3351−3360

that correlates with H + SH(A) products. However, we also note that the ratio is not zero when exciting to levels with $\langle J_b^2 \rangle = 0$, a point to which we return in Section 3.4.

This analysis also serves to confirm an earlier astrochemically relevant conclusion that the dominant S-containing products from H_2S photolysis at shorter wavelengths are S atoms, not SH radicals.[42] As noted above, most of the SH(A) products will predissociate to $S(^3P)$ atoms (channel II′), so the reported J_{KaKc}′-dependent SH(A)/SH(X) ratios are effectively S/SH ratios. As Figure 7 shows, all transitions within the $^1B_1-X^1A_1$ at transition at $\lambda \sim 129.1$ nm apart from those accessing levels with very low $\langle J_b^2 \rangle$ predominantly yield SH(A) (and thus $S(^3P)$) products. The fraction of the total oscillator strength associated with transitions to levels with low $\langle J_b^2 \rangle$ will decrease with increasing sample temperature, further reinforcing the conclusion that H_2S photolysis at these short VUV wavelengths yields S atoms rather than SH radical products.[42]

3.4. New Insights into the Photofragmentation Dynamics of H_2S When Excited at Short Wavelengths.

The results of this quantum state-selected study of H_2S fragmentation following excitation to the $^1B_1$ Rydberg state at $\lambda \sim 129.1$ nm are broadly consistent with the "big picture" description presented previously.[41] The H_2S molecules photoexcited to this Rydberg state can predissociate homogeneously, by coupling to the valence continuum of $^1A''$ symmetry, and heterogeneously, by Coriolis coupling to the $^1A'$ continuum, with relative efficiencies that depend on the rotational angular momentum of the particular J_{KaKc}′ level. Both continua are recognized as involving more than one coupled state, and recent electronic structure calculations have confirmed regions of degeneracy between the respective PESs (conical intersections between surfaces of the same symmetry, and seams of intersection between $^1A''$ and $^1A'$ surfaces at linear geometries).[41] The molecules that couple to the $^1A''$ continuum have traditionally been assumed to dissociate to H + SH(X) products (channel I) and, at sufficiently short excitation wavelengths, conceivably to some H + H + $S(^3P)$ products (channel III). The topographies of the $^1A''$ PES(s) ensure that the SH(X) products are formed in a broad range of v'', N'' levels.

Photoexcited molecules that couple to and evolve on the $^1A'$ PES(s) can experience a wider range of possible fates. Those that avoid the regions of linear configuration space that enable further nonadiabatic coupling (to the $^1A''$ PES(s)) dissociate on the $^1A'$ PES(s). The topography of the lower of these $^1A'$ surfaces encourages the rapid opening of the ∠HSH bond angle, which ultimately manifests as very high levels of rotational excitation in the resulting SH(A) products. Recent imaging studies of the $S(^1D)$ products formed when exciting at $\lambda \sim 129.1$ nm (and other neighboring wavelengths) suggest that some of the more internally excited H_2 coproducts (from channel V) arise *via* an initial H···SH bond extension. Full dissociation is frustrated by the bending-induced centrifugal barrier, however, and the departing H atom thus orbits (roams) around the SH partner. The eventual H_2 + $S(^1D)$ products then arise by intramolecular H atom transfer during a subsequent re-encounter at near H···HS configurations.[41,42] The low H + SH(X) yields observed when exciting levels with higher $\langle J_b^2 \rangle$ at $\lambda \sim 129.1$ nm suggest that, after coupling to the $^1A'$ PES(s), the probability of further nonadiabatic coupling to the $^1A''$ PES(s) is low; the balance between the H···SH stretching and ∠HSH bond angle opening forces on the $^1A'$ PES(s) is such that the dissociating molecules pass through linear configurations at H···SH separations beyond the range that supports the required nonadiabatic coupling.[41,60]

However, the present data show an additional feature that, with the benefit of hindsight, was also evident (less strongly) in the earlier parent-state-selected studies of H_2S photolysis at $\lambda \sim 139.1$ nm.[46] As Figures 2 and 5B show, excitation at $\lambda = 129.158$ nm (peak 2), resonant with the parent $0_{00}-1_{10}$ transition, clearly results in some H + SH(A) products. The H atom PHOFEX spectrum (Figure 2A) shows some H atom yield at all wavelengths in this range, which is understandable in terms of direct excitation to the underlying $^1A'$ continuum. These excitations will largely result in H + SH(A) products. But the intensity of peak 2 in the PHOFEX spectrum, and the deduced SH(A)/SH(X) product branching when exciting this feature (Figures 4A and 7), leaves little doubt that some parent population excited to the 0_{00} level of this $^1B_1$ state dissociates to H + SH(A) products.

A plausible explanation for this observation is as follows. As before, the decay of the population from the 0_{00} level starts by vibronic coupling to the $^1A''$ continuum. But, as noted previously, there are regions of configuration space at near-linear geometries where the $^1A''$ and $^1A'$ PES(s) come into near degeneracy. Such couplings have hitherto been viewed solely as a means of channeling population from the $^1A'$ PES(s) to the lower energy (viewed in terms of their respective energies in the vertical Franck−Condon region) $^1A''$ PES(s). But the photoprepared molecules in the present case access the $^1A''$ PES(s) at high total energy (∼9.6 eV relative to the ground-state minimum energy geometry), and it would not be surprising if the topography of the $^1A''$ PES(s) encouraged at least some of these molecules to sample regions of near-degeneracy with the $^1A'$ PES(s) and couple to the $^1A'$ PES(s) with nuclear momenta appropriate to access the H + SH(A) limit. Large parts of the $^1A''$ PES(s) and, to a lesser extent, the $^1A'$ PES(s) have now been reported,[40,41] and it is to be hoped that *ab initio* molecular dynamics studies may soon be forthcoming to help test and validate the foregoing mechanistic picture of the dissociation dynamics of H_2S molecules launched from near vertical Franck−Condon geometries at various different excitation energies.

The present work raises another interesting question to which theory may be able to provide insight. As noted previously, every parent J_{KaKc} level has a defined *ortho-*/*para*-nuclear spin parity, which has been shown to be conserved in the H_2 products from channel V, even in cases where these products arise *via* an initial "frustrated" H···SH bond fission and the "departing" H atom orbits (roams) around the SH partner, culminating with an intramolecular H abstraction.[46] Similar *ortho-*/*para*-nuclear spin parity conservation has been observed in the H_2 products formed from the dissociation of H_2CO molecules *via* both "transition-state" and "roaming" decay pathways.[61] The present study reiterates the decay of primary SH(A) photofragments (channels II and II′). To what extent does nuclear spin parity conservation extend to the nuclear spins of the two H atoms formed by the successive processes $H_2S(J_{KaKc}) \rightarrow H + SH(A)$, followed by $SH(A) \rightarrow H + S(^3P)$?

4. CONCLUSIONS

This study reports HRTOF studies of the S−H bond fission processes prevailing following excitation of H_2S to selected J_{KaKc}′ levels of the zero-point vibrational level of the $^1B_1(4da_1$

https://doi.org/10.1021/acs.jpca.4c01478
J. Phys. Chem. A 2024, 128, 3351−3360

← $2b_1$) Rydberg state. Analysis of the resulting $P(E_T)$ spectra reveals that all J_{KaKc}' levels predissociate to both H + SH(A) and H + SH(X) products and that the primary SH(A)/SH(X) branching ratio rises rapidly with increasing $\langle J_b^2 \rangle$, the square of the rotational angular momentum about the *b*-inertial axis in the excited state level. Such energy disposal broadly mimics that identified in earlier lower-resolution studies of H_2S photolysis at neighboring wavelengths[41] and is rationalized in terms of competing homogeneous (vibronic) and heterogeneous (Coriolis-induced) predissociation pathways involving coupling to dissociative PES(s) of, respectively, $^1A''$ and $^1A'$ symmetries. But the present data also clearly show H + SH(A) product formation when exciting the $J_{KaKc}' = 0_{00}$ and 1_{11} levels, for which $\langle J_b^2 \rangle = 0$ and Coriolis coupling to the $^1A'$ PES(s) is thus symmetry forbidden. This implies the operation of another, hitherto unrecognized, route to forming H + SH(A) products following excitation of H_2S at energies above ∼9 eV, probably involving successive nonadiabatic couplings: first (vibronic) from the Rydberg level to the $^1A''$ continuum at near vertical geometries and then (Renner−Teller enabled) from the $^1A''$ to $^1A'$ PES(s) at near-linear geometries.

Excitation at $\lambda \sim 129.1$ nm prepares H_2S molecules with $\Delta E \sim 0.7$ eV more energy than when exciting the lower energy $^1B_1(3da_1 \leftarrow 2b_1)$ member of the same Rydberg series.[46] Comparing the H + SH(A) product yields following excitation of the same J_{KaKc}' levels in the two states shows that the extra electronic energy leads to increased SH(A) product vibrational excitation, SH(A, $v' = 0$) fragments with more highly inverted rotational level population distributions, extending to higher N' quantum numbers, and a higher relative yield of SH(A) fragments *via* the newly identified non-Coriolis-induced pathway. As noted above, it is hoped that these data will stimulate future *ab initio* molecular dynamics studies designed to test, validate, and refine the foregoing mechanistic description of the photodissociation dynamics of H_2S molecules.

■ ASSOCIATED CONTENT

Supporting Information

The Supporting Information is available free of charge at https://pubs.acs.org/doi/10.1021/acs.jpca.4c01478.

H atom TOF spectra and $P(E_T)$ spectra obtained following H_2S photolysis at 129.191, 129.130, 129.124, 129.064, and 129.029 nm; simulations of the primary H + SH(A) (channel II) component to the total $P(E_T)$ spectra obtained at 129.191, 129.130, 129.064, and 129.029 nm; $P(v')$ and $P(v' = 0, N')$ distributions for the SH(A) fragments formed at these same four excitation wavelengths (PDF)

■ AUTHOR INFORMATION

Corresponding Authors

Michael N. R. Ashfold − *School of Chemistry, University of Bristol, Bristol BS8 1TS, U.K.;* orcid.org/0000-0001-5762-7048; Email: mike.ashfold@bristol.ac.uk

Kaijun Yuan − *State Key Laboratory of Molecular Reaction Dynamics and Dalian Coherent Light Source, Dalian Institute of Chemical Physics, Chinese Academy of Sciences, Dalian 116023, China; University of Chinese Academy of Sciences, Beijing 100049, China; Hefei National Laboratory, Hefei 230088, China;* orcid.org/0000-0002-5108-8984; Email: kjyuan@dicp.ac.cn

Authors

Zijie Luo − *Marine Engineering College, Dalian Maritime University, Liaoning 116026, China; State Key Laboratory of Molecular Reaction Dynamics and Dalian Coherent Light Source, Dalian Institute of Chemical Physics, Chinese Academy of Sciences, Dalian 116023, China*

Yucheng Wu − *State Key Laboratory of Molecular Reaction Dynamics and Dalian Coherent Light Source, Dalian Institute of Chemical Physics, Chinese Academy of Sciences, Dalian 116023, China; University of Chinese Academy of Sciences, Beijing 100049, China*

Shuaikang Yang − *State Key Laboratory of Molecular Reaction Dynamics and Dalian Coherent Light Source, Dalian Institute of Chemical Physics, Chinese Academy of Sciences, Dalian 116023, China; Department of Chemical Physics, School of Chemistry and Materials Science, University of Science and Technology of China, Hefei, Anhui 230026, China*

Zhenxing Li − *State Key Laboratory of Molecular Reaction Dynamics and Dalian Coherent Light Source, Dalian Institute of Chemical Physics, Chinese Academy of Sciences, Dalian 116023, China*

Wei Hua − *State Key Laboratory of Molecular Reaction Dynamics and Dalian Coherent Light Source, Dalian Institute of Chemical Physics, Chinese Academy of Sciences, Dalian 116023, China*

Zhichao Chen − *State Key Laboratory of Molecular Reaction Dynamics and Dalian Coherent Light Source, Dalian Institute of Chemical Physics, Chinese Academy of Sciences, Dalian 116023, China*

Li Che − *Department of Physics, School of Science, Dalian Maritime University, Dalian 116026, China*

Xingan Wang − *Department of Chemical Physics, School of Chemistry and Materials Science, University of Science and Technology of China, Hefei, Anhui 230026, China;* orcid.org/0000-0002-1206-7021

Complete contact information is available at: https://pubs.acs.org/10.1021/acs.jpca.4c01478

Notes

The authors declare no competing financial interest.

■ ACKNOWLEDGMENTS

The experimental work was supported by the National Natural Science Foundation of China (Grant Nos. 22241304 and 22225303), the National Natural Science Foundation of China (NSFC Center for Chemical Dynamics (Grant No. 22288201)), the Scientific Instrument Developing Project of the Chinese Academy of Sciences (Grant No. GJJSTD20220001), the Innovation Program for Quantum Science and Technology (2021ZD0303304), and the Innovation Fund Project of Dalian Institute of Chemical Physics (DICP I202112).

■ REFERENCES

(1) Yamamoto, S. *Introduction to Astrochemistry: Chemical Evolution from Interstellar Clouds to Star and Planet Formation*; Springer: Japan, 2017.

(2) Neufeld, D. A.; Godard, B.; Gerin, M.; des Forets, G. P.; Bernier, C.; Falgarone, E.; Graf, U. U.; Guesten, R.; Herbst, E.; Lesaffre, P.; et al. Sulphur-bearing Molecules in Diffuse Molecular Clouds: New Results from SOFIA/GREAT and the IRAM 30 m Telescope. *Astron. Astrophys.* **2015**, *577*, A49.

(3) Woods, P. M.; Occhiogrosso, A.; Viti, S.; Kanuchova, Z.; Palumbo, M. E.; Price, S. D. A New Study of an Old Sink of Sulphur in Hot Molecular Cores: the Sulphur Residue. *Mon. Not. R. Astron. Soc.* **2015**, *450*, 1256−1267.
(4) Kama, M.; Shorttle, O.; Jermyn, A. S.; Folsom, C. P.; Furuya, K.; Bergin, E. A.; Walsh, C.; Keller, L. Abundant Refractory Sulfur in Protoplanetary Disks. *Astrophys. J.* **2019**, *885*, 114.
(5) Fuente, A.; Rivière-Marichalar, P.; Beitia-Antero, L.; Caselli, P.; Wakelam, V.; Esplugues, G.; Rodríguez-Baras, P. M.; Navarro-Almaida, D.; Gerin, M.; Kramer, C.; et al. Gas Phase Elemental Abundances in Molecular CloudS (GEMS) VII. Sulfur Elemental Abundance. *Astron. Astrophys.* **2023**, *670*, No. A114, DOI: 10.1051/0004-6361/202244843. and references therein
(6) Goicoechea, J. R.; Pety, J.; Gerin, M.; Teyssier, D.; Roueff, E.; Hily-Blant, P.; Baek, S. Low Sulfur Depletion in the Horsehead PDR. *Astron. Astrophys.* **2006**, *456*, 565−580.
(7) Vastel, C.; Quenard, D.; Le Gal, R.; Wakelam, V.; Andrianasolo, A.; Caselli, P.; Vidal, T.; Ceccarelli, C.; Lefloch, B.; Bachiller, R. Sulphur Chemistry in the L1544 Pre-stellar Core. *Mon. Not. R. Astron. Soc.* **2018**, *478*, 5519−5537.
(8) Hily-Blant, P.; des Forets, G. P.; Faure, A.; Lique, F. Sulfur Gas-phase Abundance in Dense Cores. *Astron. Astrophys.* **2022**, *658*, A168.
(9) Riviere-Marichalar, P.; Fuente, A.; Esplugues, G.; Wakelam, V.; Le Gal, R.; Baruteau, C.; Ribas, A.; Macias, E.; Neri, R.; Navarro-Almaida, D. AB Aur, a Rosetta Stone for Studies of Planet Formation II. H_2S Detection and Sulfur Budget. *Astron. Astrophys.* **2022**, *665*, No. A61, DOI: 10.1051/0004-6361/202142906.
(10) Vidal, T. H. G.; Loison, J. C.; Jaziri, A. Y.; Ruaud, M.; Gratier, P.; Wakelam, V. On the Reservoir of Sulphur in Dark Clouds: Chemistry and Elemental Abundance Reconciled. *Mon. Not. R. Astron. Soc.* **2017**, *469*, 435−447.
(11) Oba, Y.; Tomaru, T.; Lamberts, T.; Kouchi, A.; Watanabe, N. An Infrared Measurement of Chemical Desorption from Interstellar Ice Analogues. *Nat. Astron.* **2018**, *2*, 228−232.
(12) Rodriguez-Baras, M.; Fuente, A.; Riviere-Marichalar, P.; Navarro-Almaida, D.; Caselli, P.; Gerin, M.; Kramer, C.; Roueff, E.; Wakelam, V.; Esplugues, G.; et al. Gas Phase Elemental Abundances in Molecular CloudS (GEMS) IV. Observational Results and Statistical Trends. *Astron. Astrophys.* **2021**, *648*, No. A120, DOI: 10.1051/0004-6361/202040112.
(13) Cazaux, S.; Carrascosa, H.; Caro, G. M. M.; Caselli, P.; Fuente, A.; Navarro-Almaida, D.; Riviere-Marichalar, P. Photoprocessing of H_2S on Dust Grains. Building S Chains in Translucent Clouds and Comets. *Astron. Astrophys.* **2022**, *657*, No. A100, DOI: 10.1051/0004-6361/202141861.
(14) Eberhardt, P.; Meier, R.; Krankowsky, D.; Hodges, R. R. Methanol and Hydrogen Sulfide in Comet P/Halley. *Astron. Astrophys.* **1994**, *288*, 315−329.
(15) Bockelee-Morvan, D.; Lis, D. C.; Wink, J. E.; Despois, D.; Crovisier, J.; Bachiller, R.; Benford, D. J.; Biver, N.; Colom, P.; Davies, J. K.; et al. New Molecules Found in Comet C/1995 O1 (Hale-Bopp): Investigating the Link between Cometary and Interstellar Material. *Astron. Astrophys.* **2000**, *353*, 1101−1114.
(16) Boissier, J.; Bockelee-Morvan, D.; Biver, N.; Crovisier, J.; Despois, D.; Marsden, B. G.; Moreno, R. Interferometric Imaging of the Sulfur-bearing Molecules H_2S, SO, and CS in Comet C/1995 O1 (Hale-Bopp). *Astron. Astrophys.* **2007**, *475*, 1131−1144.
(17) Biver, N.; Bockelee-Morvan, D.; Moreno, R.; Crovisier, J.; Colom, P.; Lis, D. C.; Sandqvist, A.; Boissier, J.; Despois, D.; Milam, S. N. Ethyl Alcohol and Sugar in Comet C/2014 Q2 (Lovejoy). *Sci. Adv.* **2015**, *1*, No. e1500863.
(18) Calmonte, U.; Altwegg, K.; Balsiger, H.; Berthelier, J. J.; Bieler, A.; Cessateur, G.; Dhooghe, F.; van Dishoeck, E. F.; Fiethe, B.; Fuselier, S. A.; et al. Sulphur-bearing Species in the Coma of Comet 67P/Churyumov-Gerasimenko. *Mon. Not. R. Astron. Soc.* **2016**, *462*, S253−S273.
(19) Niemann, H. B.; Atreya, S. K.; Carignan, G. R.; Donahue, T. M.; Haberman, J. A.; Harpold, D. N.; Hartle, R. E.; Hunten, D. M.; Kasprzak, W. T.; Mahaffy, P. R.; et al. The Composition of the Jovian Atmosphere as Determined by the Galileo Probe Mass Spectrometer. *J. Geophys. Res.: Planets* **1998**, *103*, 22831−22845.
(20) Irwin, P. G. J.; Toledo, D.; Garland, R.; Teanby, N. A.; Fletcher, L. N.; Orton, G. S.; Bezard, B. Detection of Hydrogen Sulfide above the Clouds in Uranus's Atmosphere. *Nat. Astron.* **2018**, *2*, 420−427.
(21) Molter, E. M.; de Pater, I.; Luszcz-Cook, S.; Tollefson, J.; Sault, R. J.; Butler, B.; de Boer, D. Tropospheric Composition and Circulation of Uranus with ALMA and the VLA. *Planet. Sci. J.* **2021**, *2*, 3.
(22) Irwin, P. G. J.; Toledo, D.; Garland, R.; Teanby, N. A.; Fletcher, L. N.; Orton, G. S.; Bezard, B. Probable Detection of Hydrogen Sulphide (H_2S) in Neptune's Atmosphere. *Icarus* **2019**, *321*, 550−563.
(23) Rivière-Marichalar, P.; Fuenta, A.; Le Gal, R.; Arabhavi, A. M.; Casaux, S.; Navarro-Almaida, D.; Ribas, A.; Mendigutia, I.; Barrado, D.; Montesinos, B. H_2S Observations in Young Stellar Disks in Taurus. *Astron. Astrophys.* **2021**, *652*, A46.
(24) Gorai, P.; Law, C.-Y.; Tan, J. C.; Zhang, Y. C.; Fedriani, R.; Tanaka, T. E. I.; Bonfand, M.; Cosentino, G.; Mardones, D.; Beltrán, M. T.; Garay, G. Astrochemical Diagnostics of the Isolated Massive ProtostarG28.20−0.05. *Astrophys. J.* **2024**, *960*, 127.
(25) Tannock, M. E.; Metchev, S.; Hood, C. E.; Mace, G. N.; Fortney, J. J.; Morley, C. V.; Jaffe, D. T.; Lupu, R. A 1.46−2.48 μm Spectroscopic Atlas of a T6 Dwarf (1060 K) Atmosphere with IGRINS: First Detections of H_2S and H_2, and Verification of H_2O, CH_4, and NH_3 Line Lists. *Mon. Not. R. Astron. Soc.* **2022**, *514*, 3160−3178.
(26) Tsai, S.-M.; Lee, E. K. H.; Powell, D.; Gao, P.; Zhang, X.; Moses, J.; Hébrard, E.; Venot, O.; Parmentier, V.; Jordon, S.; et al. Photochemically Produced SO_2 in the Atmosphere of WASP-39b. *Nature* **2023**, *617*, 483−487.
(27) Lee, L. C.; Wang, X. Y.; Suto, M. Quantitative Photoabsorption and Fluorescence Spectroscopy of H_2S and D_2S at 49−240 nm. *J. Chem. Phys.* **1987**, *86*, 4353−4361.
(28) Masuko, H.; Morioka, Y.; Nakamura, M.; Ishiguro, E.; Sasanuma, M. Absorption Spectrum of the H_2S Molecule in the Vacuum Ultraviolet Region. *Can. J. Phys.* **1979**, *57*, 745−760.
(29) Mayhew, C. A.; Connerade, J. P.; Baig, M. A.; Ashfold, M. N. R.; Bayley, J. M.; Dixon, R. N.; Prince, J. D. High-resolution Studies of the Electronic Spectra of H_2S and D_2S. *J. Chem. Soc., Faraday Trans. 2* **1987**, *83*, 417−434.
(30) Fischer, I.; Lochschmidt, A.; Strobel, A.; Niedner-Schatteburg, G.; Muller-Dethlefs, K.; Bondybey, V. E. The Non-resonant Two-photon Zero Kinetic Energy Photoelectron Spectrum from the Electronic Ground State of H_2S. *J. Chem. Phys.* **1993**, *98*, 3592−3599.
(31) Ashfold, M. N. R.; Bayley, J. M.; Dixon, R. N.; Prince, J. D. Molecular Predissociation Dynamics Revealed through Multiphoton Ionization Spectroscopy, III. New $^1A_2$ and $^1B_1$ Rydberg States in H_2S and D_2S. *Chem. Phys.* **1985**, *98*, 289−313.
(32) Ashfold, M. N. R.; Hartree, W. S.; Salvato, A. V.; Tutcher, B.; Walker, A. A Reinvestigation of the Rydberg States of H_2S and D_2S by Two-photon Resonant Multiphoton Ionisation Spectroscopy. *J. Chem. Soc., Faraday Trans.* **1990**, *86*, 2027−2034.
(33) Shiell, R. C.; Hu, X. K.; Hu, Q. J.; Hepburn, J. W. A Determination of the Bond Dissociation Energy (D_0(H−SH)): Threshold Ion-pair Production Spectroscopy (TIPPS) of a Triatomic Molecule. *J. Phys. Chem. A* **2000**, *104*, 4339−4342.
(34) Zhou, W. D.; Yuan, Y.; Chen, S. P.; Zhang, J. S. Ultraviolet Photodissociation Dynamics of the SH Radical. *J. Chem. Phys.* **2005**, *123*, No. 054330.
(35) Komasa, J.; Piszczatowski, K.; Łach, G.; Przybytek, M.; Jeziorski, B.; Pachucki, K. Quantum Electrodynamics Effects in Rovibrational Spectra of Molecular Hydrogen. *J. Chem. Theory Comput.* **2011**, *7*, 3105−3115.
(36) Linstrom, P. J.; Mallard, W. G. Neutral Thermochemical Data. *NIST Chemistry WebBook*, NIST Standard Reference Database Number 69; National Institute of Standards and Technology: Gaithersburg, MD, 2011. http://webbook.nist.gov (retrieved September 13, 2011).

https://doi.org/10.1021/acs.jpca.4c01478
J. Phys. Chem. A 2024, 128, 3351−3360

(37) Kramida, A.; Ralchenko, Y.; Reader, J. Atomic Spectroscopy Data. *NIST Atomic Spectra Database*; National Institute of Standards and Technology: Gaithersburg, MD, 2019. https://www.nist.gov.
(38) Wilson, S. H. S.; Howe, J. D.; Ashfold, M. N. R. On the Near Ultraviolet Photodissociation of Hydrogen Sulphide. *Mol. Phys.* **1996**, *88*, 841−858.
(39) Liu, X.; Hwang, D. W.; Yang, X. F.; Harich, S.; Lin, J. J.; Yang, X. M. Photodissociation of Hydrogen Sulfide at 157.6 nm: Observation of SH Bimodal Rotational Distribution. *J. Chem. Phys.* **1999**, *111*, 3940−3945.
(40) Chen, J. J.; Zhang, H. Z.; Zhou, L. S.; Hu, X. X.; Xie, D. Q. New Accurate Diabatic Potential Energy Surfaces for the Two Lowest $^1A''$ States of H_2S and Photodissociation Dynamics in its First Absorption Band. *Phys. Chem. Chem. Phys.* **2023**, *25*, 26032−26042. and references therein
(41) Zhao, Y. R.; Chen, J. J.; Luo, Z. J.; Chang, Y.; Yang, J. Y.; Zhang, W. Q.; Wu, G. R.; Crane, S. W.; Hansen, C. S.; Ding, H. B.; et al. The Vibronic State Dependent Predissociation of H_2S: Determination of all Fragmentation Processes. *Chem. Sci.* **2023**, *14*, 2501−2517. and references therein
(42) Zhou, J. M.; Zhao, Y. R.; Hansen, C. S.; Yang, J. Y.; Chang, Y.; Yu, Y.; Cheng, G. K.; Chen, Z. C.; He, Z. G.; Yu, S. R.; et al. Ultraviolet Photolysis of H_2S and its Implications for SH Radical Production in the Interstellar Medium. *Nat. Commun.* **2020**, *11*, No. 1547.
(43) Zhao, Y. R.; Chen, J. J.; Luo, Z. J.; Li, Z. X.; Yang, S. K.; Chang, Y.; An, F.; Chen, Z. C.; Yang, J. Y.; Wu, G. R.; et al. Photodissociation of H_2S: A New Pathway for the Production of Vibrationally Excited Molecular Hydrogen in the Interstellar Medium. *J. Phys. Chem. Lett.* **2022**, *13*, 9786−9792.
(44) Rose, R. A.; Orr-Ewing, A. J.; Yang, C. H.; Vidma, K.; Groenenboom, G. C.; Parker, D. H. Photodissociation Dynamics of the A $^2\sum^+$ State of SH and SD Radicals. *J. Chem. Phys.* **2009**, *130*, No. 034307.
(45) Qin, Y.; Zheng, X. F.; Song, Y.; Sun, G.; Zhang, J. S. Vibrational Energy Levels and Predissociation Lifetimes of the $A^2\sum^+$ State of SH/SD Radicals by Photodissociation Spectroscopy. *J. Chem. Phys.* **2022**, *157*, No. 134303.
(46) Zhao, Y. R.; Luo, Z. J.; Chang, Y.; Wu, Y. C.; Zhang, S.; Li, Z. X.; Ding, H. B.; Wu, G. R.; Campbell, J. S.; Hansen, C. S.; et al. Rotational and Nuclear-spin Level Dependent Photodissociation Dynamics of H_2S. *Nat. Commun.* **2021**, *12*, No. 4459.
(47) Ashfold, M. N. R.; Yuan, K. J.; Yang, X. M. Perspective: The Development and Applications of H Rydberg Atom Translational Spectroscopy Methods. *J. Chem. Phys.* **2018**, *149*, No. 080901. and references therein
(48) Luo, Z. J.; Zhao, Y. R.; Chen, Z. C.; Chang, Y.; Zhang, S.; Wu, Y. C.; Yang, J. Y.; Cheng, Y.; Che, L.; Wu, G. R.; et al. Strong Isotope Effect in the VUV Photodissociation of HOD: A Possible Origin of D/H Isotope Heterogeneity in the Solar Nebula. *Sci. Adv.* **2021**, *7*, No. eabg7775.
(49) Chang, Y.; Ashfold, M. N. R.; Yuan, K. J.; Yang, X. M. Exploring the Vacuum Ultraviolet Photochemistry of Astrochemically Important Triatomic Molecules. *Nat. Sci. Rev.* **2023**, *10*, No. nwad158.
(50) Liao, H.; Li, Z.; Yuan, D. F.; Chen, W. T.; Wang, X. A.; Yu, S. R.; Yang, X. M. Vacuum Ultraviolet Photodissociation Dynamics of $N_2O+h\nu\rightarrow N_2(X^1\sum_g^+)+O(^1S)$ in the Short Wavelength Tail of $D^1\sum^+$ band. *Chin. J. Chem. Phys.* **2022**, *35*, 860−866.
(51) Tang, L.; Chen, W. T.; Yuan, D. F.; Yu, S. R.; Yang, X. M.; Wang, X. A. Vacuum Ultraviolet Photodissociation Dynamics of OCS via the *F* Rydberg State: The $S(^3P_{J=2,1,0})$ Product Channels. *Chin. J. Chem. Phys.* **2022**, *35*, 249−256.
(52) Chang, Y.; He, Z. G.; Luo, Z. J.; Zhou, J. M.; Zhang, Z. G.; Chen, Z. C.; Yang, J. Y.; Yu, Y.; Li, Q. M.; Che, L.; et al. Application of Laser Dispersion Method in Apparatus Combining H Atom Rydberg Tagging Time-of-Flight Technique with Vacuum Ultraviolet Free Electron Laser. *Chin. J. Chem. Phys.* **2020**, *33*, 139−144.
(53) Western, C. M. PGOPHER: A Program for Simulating Rotational, Vibrational and Electronic Spectra. *J. Quant. Spectrosc. Radiat. Transfer* **2017**, *186*, 221−242.
(54) Gillis, J. R.; Edwards, T. H. Analysis of $2\nu_2$, ν_1, and ν_3 of H_2S. *J. Mol. Spectrosc.* **1981**, *85*, 55−73.
(55) Duxbury, G.; Horani, M.; Rostas, J. Rotational Analysis of Electronic Emission-Spectrum of H_2S^+ Ion Radical. *Proc. R. Soc. London, Ser. A* **1972**, *331*, 109−137, DOI: 10.1098/rspa.1972.0167.
(56) Yuan, K. J.; Cheng, Y.; Cheng, L.; Guo, Q.; Dai, D. X.; Wang, X. Y.; Yang, X. M.; Dixon, R. N. Nonadiabatic Dissociation Dynamics in H_2O: Competition between Rotationally and Non-rotationally Mediated Pathways. *Proc. Natl. Acad. Sci. U.S.A.* **2008**, *105*, 19148−19153.
(57) Qin, Y.; Zheng, X. F.; Song, Y.; Sun, G.; Zhang, J. S. Predissociation Dynamics of the $A^2\sum^+$ State of SH Radical: Fine-structure State Distributions of the $S(^3P_J)$ Products. *J. Chem. Phys.* **2023**, *159*, No. 141103.
(58) Chang, Y.; Yu, Y.; An, F.; Luo, Z. J.; Quan, D. H.; Zhang, X.; Hu, X. X.; Li, Q. M.; Yang, J. Y.; Chen, Z. C.; et al. Three Body Photodissociation of the Water Molecule and its Implications for Prebiotic Oxygen Production. *Nat. Commun.* **2021**, *12*, No. 2476.
(59) Schnieder, L.; Meier, W.; Welge, K. H.; Ashfold, M. N. R.; Western, C. M. Photodissociation Dynamics of H_2S at 121.6 nm and a Determination of the Potential Energy Function of $SH(A^2\sum^+)$. *J. Chem. Phys.* **1990**, *92*, 7027−7037.
(60) Cook, P. A.; Langford, S. R.; Dixon, R. N.; Ashfold, M. N. R. An Experimental and Ab Initio Reinvestigation of the Lyman-α Photodissociation of H_2S and D_2S. *J. Chem. Phys.* **2001**, *114*, 1672−1684.
(61) Quinn, M. S.; Nauta, K.; Kable, S. H. Disentangling the H_2 E,F$(^1\sum_g^+)$ $(v' = 0-18)$ ← X$(^1\sum_g^+)$ $(v'' = 3-9)$ (2 + 1) REMPI Spectrum via 2D Velocity-mapped Imaging. *Mol. Phys.* **2021**, *119*, No. e1836412.

https://doi.org/10.1021/acs.jpca.4c01478
J. Phys. Chem. A 2024, 128, 3351−3360